J. Fluid Mech. (2013), *vol.* 730, *pp.* 464–490.
doi:10.1017/jfm.2013.348

Oceanic wave-balanced surface fronts and filaments

James C. McWilliams[1],† **and Baylor Fox-Kemper**[2]

[1]Department of Atmospheric and Oceanic Sciences, University of California, Los Angeles, CA 90095-1565, USA

[2]Department of Atmospheric and Oceanic Sciences, University of Colorado, Boulder, CO 80309-0311, USA

(Received 29 October 2012; revised 9 April 2013; accepted 3 July 2013; first published online 1 August 2013)

A geostrophic, hydrostatic, frontal or filamentary flow adjusts conservatively to accommodate a surface gravity wave field with wave-averaged, Stokes-drift vortex and Coriolis forces in an altered balanced state. In this altered state, the wave-balanced perturbations have an opposite cross-front symmetry to the original geostrophic state; e.g. the along-front flow perturbation is odd-symmetric about the frontal centre while the geostrophic flow is even-symmetric. The adjustment tends to make the flow scale closer to the deformation radius, and it induces a cross-front shape displacement in the opposite direction to the overturning effects of wave-aligned down-front and up-front winds. The ageostrophic, non-hydrostatic, adjusted flow may differ from the initial flow substantially, with velocity and buoyancy perturbations that extend over a larger and deeper region than the initial front and Stokes drift. The largest effect occurs for fronts that are wider than the mixed layer deformation radius and that fill about two-thirds of a well-mixed surface layer, with the Stokes drift spanning only the shallowest part of the mixed layer. For even deeper mixed layers, and especially for thinner or absent mixed layers, the wave-balanced adjustments are not as large.

Key words: ocean processes, surface gravity waves, waves in rotating fluids

1. Introduction

The persistent currents in the ocean are unstable and generate mesoscale eddies. In turn the eddies have surface currents with horizontal strain fields that act on horizontal density gradients to form elongated surface fronts and filaments on a smaller spatial scale (called submesoscale). Fronts have narrow zones with a one-signed density gradient across their axis, while filaments have a central density extremum on their axis; both configurations develop along-axis currents in approximately hydrostatic, geostrophic momentum balance. In the absence of further mesoscale straining and dissipative processes (e.g. boundary layer turbulence), these are approximately steady states of flow and density stratification, although they may often be unstable steady states.

This depiction neglects the surface-layer influence of surface gravity waves that are also prevalent. The waves induce a surface-trapped Lagrangian mean current in the

† Email address for correspondence: jcm@atmos.ucla.edu

direction of their propagation, called Stokes drift $\boldsymbol{u}_s$. Stokes drift provides a vortex stretching (also called the vortex force) and a Stokes Coriolis force that influence the evolution of the ambient currents. In addition to these new forces, the scalar fields whose distribution specifies a geostrophic, hydrostatic flow (i.e. buoyancy and potential vorticity) are advected by the sum of the Stokes and the wave-averaged Eulerian velocity. In this paper we extend the geostrophic, hydrostatic balance that is germane to oceanic submesoscale surface fronts and filaments, so that wave effects can be incorporated in a generalized balanced stationary state.

The relevant dynamical regime comprises rotating, stratified flows near the top of the ocean. This defines a regime parameter, the Rossby number $\mathscr{R} = V/f\ell$ (with V a characteristic frontal velocity scale, ℓ its width, and f the Coriolis frequency), that is typically quite small for basin-scale and mesoscale currents and often is not large even for submesoscale currents. The density field is usually stably stratified in the upper ocean – often weakly so in the 'mixed layer' created by boundary layer turbulence, but strongly so in the pycnocline below. Surface waves develop in response to wind generation, with typical equilibrium conditions characterized by a Stokes drift with magnitude (V_s) larger than the current speed (V) and vertical length scale (h_s) smaller than the scale of the currents or stratification (h). The parameter $\epsilon = V_s h/(f\ell h_s)$ quantifies the relative size of the wave-induced effects in the adjusted front.

Conservative geostrophic balance is well accepted as relevant for surface fronts observed in the ocean, and a conservative generalization to encompass wave balance should be at least as relevant. It is common diagnostic practice to decompose sub-inertial surface currents into geostrophic and Ekman-layer components, assuming a linear superposition of their respectively conservative and non-conservative (turbulent) dynamics, at least partly justified by a difference in their horizontal scales. Nevertheless, frontal flows may have significant modifications by turbulent mixing, and this needs further investigation, for example using large-eddy simulation models with full wave-averaged dynamics, where the conservative wave-adjusted states obtained here could be used for consistent initialization. The conservative theory including surface wave effects presented in this paper is a useful first step on this path.

In § 2 we specify the wave-averaged dynamical equations, then identify steady frontal and filamentary flow configurations without surface waves, and next derive the generalized balance relations in the presence of waves. We posit a conservative adjustment process for the evolution between these two configurations. In § 3 we perform an asymptotic analysis for small $\mathscr{R}$ to explicitly pose the adjustment problem, and we identify another relevant parameter, ϵ, which is typically larger than $\mathscr{R}$ in the ocean (figure 1). In § 4 we solve the adjustment problem at leading order in $\mathscr{R}, \epsilon \ll 1$, for both frontal and filamentary flows with both uniform stratification and a surface mixed layer. In § 5 we extend these solutions to finite ϵ while retaining $\mathscr{R} \ll 1$, consistent with the observational estimate in figure 1. We do not consider cases here with $\mathscr{R} \sim 1$, despite their importance for the oceanic submesoscale, because the nonlinear equations that result are less tractable. In § 6 we give a summary and discussion of some further implications of this phenomenon.

2. Wave-averaged dynamics and frontal balance

In the presence of a steady, horizontally uniform surface gravity wave field, conservative wave-averaged Boussinesq fluid equations for the current $\boldsymbol{u}$ are

$$\partial_t \boldsymbol{u} + (f\hat{\boldsymbol{z}} + \boldsymbol{\omega}) \times (\boldsymbol{u} + \boldsymbol{u}_s) = -\boldsymbol{\nabla}(\pi^\dagger + \tfrac{1}{2}\boldsymbol{u}^2) + b^\dagger \hat{\boldsymbol{z}}, \tag{2.1a}$$

$$\partial_t b^\dagger + (\boldsymbol{u} + \boldsymbol{u}_s) \cdot \boldsymbol{\nabla} b^\dagger = 0, \quad \boldsymbol{\nabla} \cdot \boldsymbol{u} = 0 \tag{2.1b}$$

(Craik & Leibovich 1976; Gjaja & Holm 1996; McWilliams, Restrepo & Lane 2004). Here f is the Coriolis frequency, and we have made the 'traditional approximation'

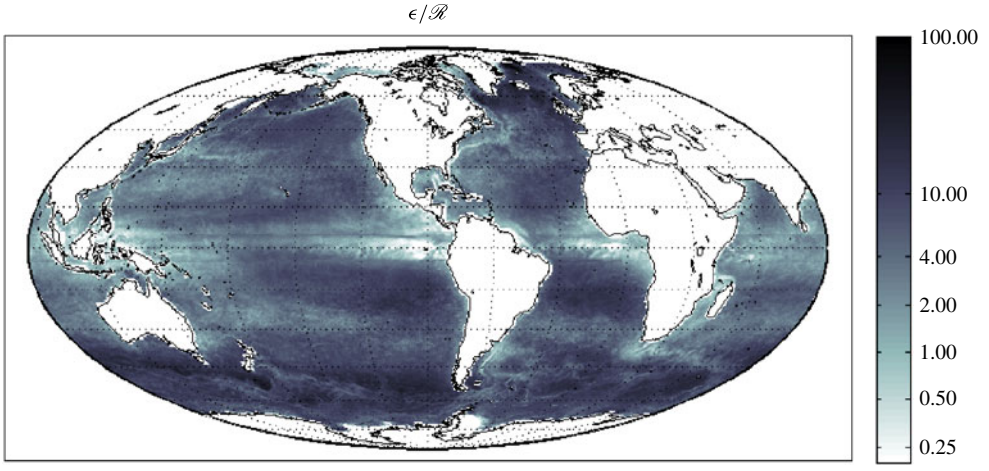

FIGURE 1. (Colour online) Estimated ratio $\epsilon/\mathscr{R} \approx (|\boldsymbol{u}_s \cdot \boldsymbol{u}|h)\,/(|\boldsymbol{u}|^2 h_s)$ governing the relative importance of Stokes effects versus nonlinearity. Eulerian velocity ($\boldsymbol{u}$) is taken as the AVISO weekly satellite geostrophic velocity or $-\boldsymbol{u}_s$ (for anti-Stokes flow) if $|\boldsymbol{u}_s| > |\boldsymbol{u}|$. The front/filament depth (h) is estimated as the mixed layer depth from the de Boyer Montégut *et al.* (2004) climatology. An exponential fit to the Stokes drift of the upper 9 m projected onto the AVISO geostrophic velocity provides $\boldsymbol{u}_s \cdot \boldsymbol{u}$ and h_s. Stokes drift is taken from the Wave Watch 3 simulation described in Webb & Fox-Kemper (2011). $\boldsymbol{u}, \boldsymbol{u}_s$, and h_s are all for the year 2000, while h is from a climatology of observations over 1961–2008. The year 2000 average of $\epsilon/\mathscr{R}$ is shown.

by neglecting the locally horizontal projection of Earth's rotation vector; $\boldsymbol{\omega} = \boldsymbol{\nabla} \times \boldsymbol{u}$ is the vorticity; $\boldsymbol{u}_s(z)$ is the waves' Lagrangian-mean Stokes-drift profile, and $\boldsymbol{u} + \boldsymbol{u}_s$ is the total wave-averaged Lagrangian-mean velocity for waves and currents; z is the vertical coordinate parallel to gravity and the rotation axis, and $\hat{\boldsymbol{z}}$ is its unit vector; the total buoyancy field is $b^\dagger = -(\rho - \rho_0)g/\rho_0$, and $\pi^\dagger$ is a generalized pressure field that additionally includes the Bernoulli head from averaging over the wave fluctuations, normalized by a spatially constant mean density ρ_0. These equations can be combined to yield Lagrangian-advective conservation of Ertel potential vorticity q,

$$\partial_t q + (\boldsymbol{u} + \boldsymbol{u}_s) \cdot \boldsymbol{\nabla} q = 0, \quad q = (f\hat{\boldsymbol{z}} + \boldsymbol{\omega}) \cdot \boldsymbol{\nabla} b^\dagger, \tag{2.2}$$

as a complement to the advective conservation of $b^\dagger$ in (2.1).

A well-known and importantly oceanic steady solution of (2.1) is a geostrophic, hydrostatic, parallel flow, $\boldsymbol{u} = v_0(x, z)\hat{\boldsymbol{y}}$, with associated $\pi_0(x, z)$ and $b_0(x, z)$, when there are no waves (i.e. $\boldsymbol{u}_s = 0$):

$$f v_0 = \partial_x \pi_0, \quad \partial_z \pi_0 = b_0 \quad \Rightarrow f \partial_z v_0 = \partial_x b_0. \tag{2.3}$$

The last relation is derived from the first two and is called thermal wind balance. Here (x, y, z) and (u, v, w) are Cartesian coordinates and velocities. We assume f is spatially uniform and oriented in the vertical for simplicity. We further assume that b_0 is additive on top of a background stratification profile, $\overline{b}(z) = \int_z N^2(z')\,\mathrm{d}z'$, where $N(z)$ is the buoyancy frequency, which is in hydrostatic balance with a mean background pressure, $\overline{\pi}(z)$. Henceforth we denote by b the dynamical buoyancy increment to $\overline{b}$ in a decomposition of the total buoyancy, $b^\dagger = \overline{b} + b$ (ditto for π). We restrict our attention

to statically stable flows, with

$$\partial_z b^\dagger = N^2(z) + \partial_z b(x,z) \geqslant 0 \tag{2.4}$$

at all locations. The associated two-dimensional q field is

$$q = (f + \partial_x v)(N^2 + \partial_z b) - \partial_z v \partial_x b = fN^2 + N^2 \partial_x v + f\partial_z b + J(v,b), \tag{2.5}$$

where $J(\alpha,\beta) = \partial_x\alpha\partial_z\beta - \partial_z\alpha\partial_x\beta$ is the two-dimensional Jacobian differential operator. In the absence of waves $q = q_0$ is evaluated using $v = v_0$ and $b = b_0$.

This hydrostatic, geostrophic balanced flow has the property that when $b_0(x,z)$ and $q_0(x,z)$ are specified, v_0 is then fully determined by 'inversion' of the balance relations under the constraint that $v_0 \to 0$ in the far field. Invertibility is a general property of balanced flows (Gent & McWilliams 1983). We now seek to generalize the balance relations for currents in the presence of surface waves.

Assume there is an obliquely incident, steady, conservative surface gravity wave field with a Stokes drift velocity, $\boldsymbol{u}_s = (u_s(z), v_s(z), 0)$. This permits a differently balanced steady two-dimensional solution of (2.1). In the cross-front direction, it has velocity $u = -u_s(z)$. This is an 'anti-Stokes' Eulerian flow that opposes the Stokes drift; because $f \neq 0$ and the pressure does not vary in y, the only term that can balance the Stokes Coriolis term (fu_s) in the $\hat{\boldsymbol{y}}$ momentum equation is the Eulerian Coriolis term (fu). The rest of the wave-adjusted two-dimensional flow is the along-front velocity $v = v(x,z)$ and vertical velocity $w = 0$; so the Lagrangian circulation in the cross-frontal plane is zero. The steady $\hat{\boldsymbol{x}}$, $\hat{\boldsymbol{z}}$ momentum equations are

$$-f(v + \underbrace{v_s}_{\text{SC}}) = -\partial_x \pi + \underbrace{v_s \partial_x v}_{\text{SV}}, \quad \partial_z \pi = b + \underbrace{v_s \partial_z v}_{\text{SV}} \Rightarrow f\partial_z(v + \underbrace{v_s}_{\text{SC}}) = \partial_x b - \underbrace{(\partial_z v_s)\partial_x v}_{\text{SV}}. \tag{2.6}$$

No momentum advection is present in these balances. The Stokes Coriolis (SC) and Stokes vortex (SV) forces now interfere with geostrophic, hydrostatic balance, and the thermal wind relation and down-front vorticity balance are now unbalanced by Stokes Coriolis (SC) and Stokes vortex (SV) tilting terms. The $\hat{\boldsymbol{y}}$ momentum, buoyancy conservation, and continuity equations in (2.1) are satisfied trivially for $b = b(x,z)$, due to the anti-Stokes flow and combined advection by Eulerian and Stokes velocities in (2.1)–(2.2). Notice, however, that the system (2.6) is undetermined, with two independent equations for three fields, (v, π, b). The associated two-dimensional $q = q(x,z)$ field is given by (2.5).

We resolve the indeterminacy by posing the wave-balanced front problem as one of conservative adjustment of the waveless balanced front (2.3), analogous to the geostrophic adjustment of an initially unbalanced flow. That is, we assume an initial front $v_0(x,z)$ and an adiabatic adjustment to the arrival of the surface waves, reaching a final steady flow $v(x,z)$ through a transient stage of advective rearrangement of the material parcels and radiation of internal inertia-gravity waves. This type of analysis using conservation during material parcel displacement is more fully explained in McWilliams 2006 (§ 4.3).

This concept also assumes that the spatially and temporally variable current does not alter the surface waves, consistent with an asymptotic time scale separation and a small ratio between current and wave propagation speeds (McWilliams *et al.* 2004). Lagrangian-advective conservation of q and total buoyancy, $\overline{b} + b$, between the initial and final states is expressed by

$$q(x,z) = q_0(x_0,z_0), \quad (\overline{b} + b)(x,z) = (\overline{b} + b_0)(x_0,z_0) \tag{2.7}$$

with cross-frontal and vertical parcel displacement fields

$$(\xi, \zeta)(x, z) = (x - x_0(x, z), z - z_0(x, z)), \tag{2.8}$$

respectively. Thus, (x_0, z_0) are the initial coordinates of a parcel in the frontal plane, and (x, z) are its final coordinates. Volume conservation between initial and final states requires that the Jacobian of the transformation, $|\partial(x_0, z_0)/\partial(x, z)|$, be equal to unity, or

$$\partial_x \xi + \partial_z \zeta = J(\xi, \zeta), \tag{2.9}$$

where the operator $J(a, b) = \partial_x a \partial_z b - \partial_z a \partial_x b$. Equations (2.7)–(2.9) resolve the indeterminacy of (2.6) to determine (v, π, b) given f, N^2, (v_0, π_0, b_0), and v_s. While other wave-balanced solutions to (2.6) do exist – even such extreme alternatives as $v = 0$ or $v = -v_s$ – they require that an unspecified, hence arbitrary, non-conservative process would accompany the wave adjustment, so they are less physically plausible than the conservative solution chosen here. Exploring simulations of the wave-averaged equations (2.1) with varying initial conditions, wave forcing, and non-conservative forces (as in Hamlington *et al.* 2013), may reveal whether other plausible end states exist.

We focus on fronts and filaments concentrated both near the mean sea surface at $z = 0$ and near a horizontal centre at $x = 0$; i.e. these are flows in which $v_0 \to 0$ as either $z \to -\infty$ or $x \to \pm\infty$. The ocean has a free surface at an elevation of $z = \eta(x)$. It is a material surface, so we can write $\eta(x) = \eta_0(x) + \zeta(x, \eta)$. We Taylor-expand this condition in z about the mean sea level, i.e. $\eta \approx \eta_0 + \zeta(x, 0)$. This assumes that the vertical scale of interior variation within the front is large compared to the surface elevation variation. The initial frontal flow is in geostrophic balance at the mean sea level, i.e. $f v_0(x, 0) = \partial_x \pi_0(x, 0)$. The total pressure is a constant at the free surface if the atmospheric pressure is constant on the scale of the front, so

$$\pi(x, 0) + P(x) \approx g\eta(x), \tag{2.10}$$

where P is a wave-averaged correction to π in the Taylor series expansion about mean sea level (McWilliams *et al.* 2004; § 9.3). In particular, the initial front without waves satisfies $\pi_0(x, 0) = g\eta_0(x)$. Consistent with the conservative dynamics in (2.1), no surface boundary condition on tangential stress is included.

3. Asymptotic analysis

The PDE system (2.6)–(2.9) is nonlinear with spatially variable coefficients. A degree of simplification is achieved with an asymptotic-approximation-based small Rossby number, $\mathscr{R} \ll 1$. We denote characteristic scales for the waveless front in (2.3) by velocity V, horizontal width ℓ, vertical extent h, stratification frequency in the pycnocline $\mathscr{N}$, and rotation rate f. In the usual way, $\mathscr{R} = V/f\ell$. The Burger number is $\mathscr{B} = (\mathscr{N}h/f\ell)^2$, and we assume it is $O(1)$. By geostrophic, hydrostatic balance the pressure and buoyancy scales are $\Pi = Vf\ell$ and $B = Vf\ell/h$. Furthermore, because $\boldsymbol{u}_s$ often has larger surface speed V_s and smaller vertical scale h_s compared to a surface front, we define the parameters

$$\mu \equiv La^{-2} = V_s/V \quad \text{and} \quad \lambda = h/h_s, \tag{3.1}$$

with the expectation that typically $\mu, \lambda \geqslant 1$, so $La \leqslant 1$. The parameter La is similar to the 'turbulent Langmuir number' (McWilliams, Sullivan & Moeng 1997), except that here it is defined in terms of the frontal speed V instead of the friction velocity u_* that is relevant to the wind–wave turbulent boundary layer. (These are different from the

laminar Langmuir number used in viscous theories of Langmuir circulation (Leibovich 1983).)

We non-dimensionalize the variables and equations using the frontal scales. Henceforth, all quantities are non-dimensional. We decompose the dependent variables as follows:

$$v = v_0 - \mu v_s + \epsilon v', \quad b = b_0 + \epsilon b', \quad \pi = \pi_0 + \epsilon \pi', \quad (\xi, \zeta) = \epsilon \mathscr{R}(\xi', \zeta'), \tag{3.2}$$

where the parcel displacements are non-dimensionalized by (ℓ, h). By substitution of (3.2) into the wave-balanced equations (2.6)–(2.9) and removal of the zeroth-order balances (2.3), the problem is recast in terms of the primed fields that are the rescaled adjustment departures from the initial, waveless front plus an anti-Stokes horizontal velocity. For small ϵ, the leading terms in the equations are well-ordered with the choice

$$\epsilon = \mu\lambda\mathscr{R} = \frac{\lambda\mathscr{R}}{La^2} = \frac{V_s h}{f\ell h_s}. \tag{3.3}$$

After non-dimensionalization and factoring the leading-order scaling amplitudes, the wave-balanced equations (2.6)–(2.9) are

$$\left.\begin{array}{lll} \text{Momentum:} & \partial_z v' - \partial_x b' + S_s \partial_x v_0 & = \epsilon \mathscr{P}' \\ \text{Potential vorticity:} & N^2 \partial_x v' + \partial_z b' + (\partial_z N^2)\zeta' + S_s \partial_x b_0 & = \epsilon \mathscr{Q}' \\ \text{Buoyancy:} & b' + N^2 \zeta' & = \mathscr{R}\mathscr{T}' \\ \text{Volume:} & \partial_x \xi' + \partial_z \zeta' & = \epsilon \mathscr{R}\mathscr{W}' \end{array}\right\}. \tag{3.4}$$

Here $S_s(z)$ is the normalized along-front Stokes shear $\partial_z v_s(z)$ (whose dimensional scale is $V_s/h_s = \mu\lambda V/h$), and $N(z)$ is now the non-dimensional buoyancy frequency whose value approaches 1 in the pycnocline. The left sides comprise a forced linear system for the primed variables with spatially variable coefficients only dependent on $N^2(z)$, which we assume on physical grounds to be a positive smooth function. The right sides are higher-order corrections, and they can be neglected in the leading-order asymptotic model. If these further corrections are of interest, we can evaluate their dependences on the primed variables by successive iterative corrections of the left-side solution (i.e. $Lg'^n = R[g'^{n-1}]$, $n = 2, 3, \ldots$, schematically), with convergence expected for $\mathscr{R}$ and ϵ not too large. The right sides in (3.4) are defined by

$$\epsilon \mathscr{P}' = -\epsilon S_s \partial_x v' \sim \epsilon, \tag{3.5a}$$

$$\begin{aligned} \epsilon \mathscr{Q}' = {} & -\epsilon S_s \partial_x b' - \mathscr{R}\left(J(v_0, b') + J(v', b_0) + \epsilon J(v', b')\right) \\ & + \frac{1}{\epsilon\mathscr{R}} \int_z^{z-\epsilon\mathscr{R}\zeta'} \left[\partial_z N^2(z') - \partial_z N^2(z)\right] \mathrm{d}z' \\ & + \frac{1}{\epsilon}\left(N^2 \partial_x v_0 + \partial_z b_0 + \mathscr{R} J(v_0, b_0)\right)\Big|_{(x,z)}^{(x-\epsilon\mathscr{R}\xi', z-\epsilon\mathscr{R}\zeta')} \sim \epsilon, \mathscr{R}, \end{aligned} \tag{3.5b}$$

$$\mathscr{R}\mathscr{T}' = \frac{1}{\epsilon\mathscr{R}} \int_z^{z-\epsilon\mathscr{R}\zeta'} \left[N^2(z') - N^2(z)\right] \mathrm{d}z' + \frac{1}{\epsilon} b_0 \Big|_{(x,z)}^{(x-\epsilon\mathscr{R}\xi', z-\epsilon\mathscr{R}\zeta')} \sim \mathscr{R} \tag{3.5c}$$

$$\epsilon\mathscr{R}\mathscr{W}' = \epsilon\mathscr{R} J(\xi', \zeta') \sim \epsilon\mathscr{R}. \tag{3.5d}$$

Here we use the notation $p|_a^b = p(b) - p(a)$. For each right-side term we indicate its leading asymptotic order in $\mathscr{R}$ and ϵ with the $\sim$ symbol at the end. The subtraction terms in the integrands in $\mathscr{Q}'$ and $\mathscr{T}'$ (i.e. $\int \partial_z N^2(z)\,\mathrm{d}z'$ and $\int N^2(z)\,\mathrm{d}z'$, respectively)

are identical to the left-side terms proportional to ζ' in their corresponding second and third equations in (3.4); the use of these identities allows us to separate leading- and higher-order contributions.

For localized initial flows in $v_0(x,z)$ (§ 2), we choose far-field boundary conditions such that the adjustment fluctuations are vanishingly small,

$$v', b', \zeta', \partial_x \xi' \to 0 \quad \text{as } x \to \pm\infty, z \to -\infty. \tag{3.6}$$

These include the possibility of a horizontally uniform displacement profile $\xi'(z)$ in the horizontal far field. As a further localization condition, we constrain the fluctuations to have zero overall horizontal displacement by setting $\xi'(\infty,z) + \xi'(-\infty,z) = 0$ at all depths. In § 4 we will see that this determines an x-integration constant for each z.

With a dimensional geostrophic frontal scale of $fV\ell/g$ for η, the non-dimensional surface elevation anomaly (i.e. minus an area average) is

$$\eta(x) \approx \eta_0(x) + \epsilon \mathscr{B}_{ext} \zeta'(x,0), \quad \mathscr{B}_{ext} = \frac{gh}{f^2\ell^2} \tag{3.7}$$

after linearization about the mean sea level. $\mathscr{B}_{ext}$ is an 'external' Burger number based on the air-sea density difference (rather than the internal density stratification in $\mathscr{B}$), and it has a very large value for the ℓ values associated with mesoscale and submesoscale flows, i.e. $\mathscr{B} = (L_{ext}/\ell)^2$ with L_{ext} an external deformation radius. Furthermore, the free surface condition of constant pressure (2.10) is

$$\pi_0 + \epsilon\pi' + \frac{\epsilon}{\lambda}\mathscr{P} = \eta = \eta_0 + \epsilon \mathscr{B}_{ext}\zeta' \quad \text{at } z = 0 \tag{3.8}$$

after non-dimensionalization by the geostrophic frontal scales, substitution of (3.2), and recognition that $\mathscr{P}$ has a dimensional scale of $V_s V$ for the wave–current interaction component that is spatially variable in the present problem (McWilliams *et al.* 2004). This has a frontal hydrostatic balance of $\pi_0(x,0) = \eta_0(x)$ without waves, but it is ill-ordered with waves for the adjustment fields at $O(\epsilon)$ when $\mathscr{B}_{ext} \gg 1$. This formally implies that, in the x-momentum balance for the adjustment fields, the pressure gradient $\partial_x\pi'$ at the surface associated with ζ' is large compared to the v' Coriolis force by the factor $\mathscr{B}_{ext}$. Therefore, to avoid an ill-ordered balance with a non-trivial pressure force, we must choose a surface boundary condition of

$$\zeta' = 0 \quad \text{at } z = 0. \tag{3.9}$$

This is a 'rigid lid' approximation for the adjustment fields. In the wave-averaged equations for the present problem, the effects of surface gravity waves appear via the externally-imposed Stokes drift, and therefore a wave-averaged free surface displacement is not essential to include these effects.

Inserting (3.9) into the buoyancy conservation relation in (3.4)–(3.5), we obtain the equivalent surface condition on b',

$$b'(x,0) = \mathscr{R}\mathscr{T}'(x,0) = \frac{1}{\epsilon} b_0 \Big|_{(x,0)}^{(x-\epsilon\mathscr{R}\xi'(x,0),0)} \sim \mathscr{R}. \tag{3.10}$$

The static stability constraint (2.4) has the non-dimensional form of

$$\frac{\mathscr{B}}{\mathscr{R}} N^2(z) + \partial_z b_0(x,z) + \epsilon \partial_z b'(x,z) \geqslant 0. \tag{3.11}$$

4. Leading-order wave adjustment

We analyse the forced linear system (3.4) with zero right sides that is the balanced frontal adjustment to the surface gravity waves to leading order in $\epsilon, \mathscr{R} \ll 1$. We proceed by eliminating the other fields in terms of b'. The buoyancy conservation relation gives

$$\zeta' = -\frac{1}{N^2} b'. \tag{4.1}$$

The continuity relation implies a two-dimensional non-divergent displacement vector, so we define a rotational potential with $\xi' = -\partial_z \chi'$, $\zeta' = \partial_x \chi'$, and from (4.1),

$$\chi'(x, z) = -\frac{1}{N^2} \int_0^x b'(x', z)\, \mathrm{d}x' + \chi_0'(z). \tag{4.2}$$

Using the displacement localization condition after (3.6), we determine the reference profile as

$$\chi_0'(z) = \frac{1}{2N^2} \int_0^\infty \left(b'(x', z) - b'(-x', z) \right) \mathrm{d}x'. \tag{4.3}$$

We substitute for ζ' in the potential vorticity relation and obtain

$$\partial_x v' + \partial_z \left(\frac{b'}{N^2} \right) = -\frac{S_s}{N^2} \partial_x b_0. \tag{4.4}$$

Finally, we eliminate v' between the thermal wind imbalance relation (2.6) and (4.4) to obtain a single, second-order, elliptic equation for b':

$$\partial_x^2 b' + \partial_z^2 \left(\frac{b'}{N^2} \right) = \mathscr{F}' \equiv S_s \partial_x^2 v_0 - \partial_z \left(\frac{S_s}{N^2} \partial_z v_0 \right). \tag{4.5}$$

The right-side forcing is from the vortex force. The left-side operator is well-conditioned because $N^2 > 0$ by assumption. The boundary conditions for (4.5) from (3.6) and (3.10) are $b' = 0$ at $z = 0$ and $b' \to 0$ in the far field. Once b' is known, we evaluate χ' from (4.2) and v' from the x-integral of (4.4),

$$v' = -\int_{-\infty}^x \left[\partial_z \left(\frac{b'}{N^2} \right) + \frac{S_s}{N^2} \partial_z v_0 \right] \mathrm{d}x', \tag{4.6}$$

using the boundary condition $v' \to 0$ as $x \to -\infty$. The boundary conditions for (4.5) are $b' \to 0$ as $z \to -\infty$ and $x \to \pm\infty$, as for the frontal flow itself, plus the surface condition, $b' = 0$ at $z = 0$. Alternatively, a similar elliptic equation for v' alone can be found, but the surface boundary condition is not as simple as for b'.

The leading-order system for the wave-balanced adjustment is linear in the adjustment fields, $\boldsymbol{u}_s$ and v_0. In particular, a change in sign for either $\boldsymbol{u}_s$ or v_0 yields oppositely signed adjustment fields. If $v_0(x, z)$ has a simple reflection symmetry about $x = 0$ – i.e. even for a front and odd for a filament – then b_0 has the opposite symmetry by geostrophic balance. The leading-order system in this section also has symmetric solutions for the adjustment fields. For a symmetric front, v', χ', and ξ' have odd symmetry while b' and ζ' have even symmetry, and *vice versa* for a symmetric filament. With the higher-order corrections (§ 5), these symmetries do not hold.

4.1. *Constant N^2*

In the special case of $N^2(z)$ constant with depth (i.e. non-dimensional $N = \mathscr{B}^{1/2}$), the boundary value problem (4.5) is a two-dimensional Poisson equation with a homogeneous Dirichlet boundary condition. The solution for this in a lower half-plane domain geometry is known in terms of its Green's function (Guenther & Lee 1996):

$$b' = \frac{1}{4\pi}\int_{-\infty}^{\infty} \mathrm{d}\tilde{x} \int_{-\infty}^{0} (\mathscr{B}^{1/2}\,\mathrm{d}\tilde{z}) \ln\left[\frac{r^2(\tilde{x},\tilde{z})}{r^2(\tilde{x},-\tilde{z})}\right] \mathscr{F}'(\tilde{x},\tilde{z}), \tag{4.7}$$

with $r^2 = (x-\tilde{x})^2 + \mathscr{B}(z-\tilde{z})^2$. The Green's function is $\ln[r]$ in an unbounded domain, and the combination $\ln[r^2(\tilde{x},\tilde{z})] - \ln[r^2(\tilde{x},-\tilde{z})]$ satisfies the boundary condition of $b' = 0$ at $z = 0$ through the use of an image point above the $z = 0$ surface. In this leading-order, constant-N limit, the only parameters are $\mathscr{B}$ and λ, both here and in the diagnostic formulas (4.2) for χ' and (4.6) for v'. We evaluate (4.7) by numerical quadrature using second-order discretization.

The static stability constraint (3.11) sets a limit on the minimum allowable stratification. For example, with constant stratification and the frontal flow defined in (4.8) without any wave adjustment, this lower limit is $\mathscr{B} \geqslant \sqrt{\pi}/2\mathscr{R}$. This limitation on the stratification, frontal flow, and wave adjustment formally does not apply at leading order as $\mathscr{R}, \epsilon \to 0$, but for finite parameter values and a given frontal flow it will limit both the minimum N^2 and a wave-response amplitude consistent with conservative adjustment.

4.1.1. *Front*

We define a simple initial frontal flow and balanced buoyancy anomaly by

$$v_0(x,z) = \mathrm{e}^{-x^2+z}, \quad b_0(x,z) = \frac{\sqrt{\pi}}{2}\mathrm{erf}[x]\mathrm{e}^{z}. \tag{4.8}$$

This is a step in b_0 towards lighter water near the surface for $x > 0$ and a positive, surface-trapped jet in v_0 (figure 2). The maximum velocity is equal to one at $(0,0)$, and the maximum b_0 is $\sqrt{\pi}/2 = 0.89$ at $(\infty, 0)$; v_0 is even in x, and b_0 is odd. With this symmetry the evaluation of (4.7) can be shortened by restricting the $\tilde{x}$ integration to the positive half-line and replacing the logarithmic argument with $r^2(\tilde{x},\tilde{z})r^2(-\tilde{x},\tilde{z})r^2(\tilde{x},-\tilde{z})r^2(-\tilde{x},-\tilde{z})$.

Without loss of generality because of the sign-symmetry of S_s in (4.5) and (4.6), we define the Stokes drift with a positive down-front component ($v_s > 0$). The Stokes shear profile is taken to be

$$S_s(z) = \mathrm{e}^{\lambda z}. \tag{4.9}$$

This shape corresponds to a monochromatic surface wave with dimensional wavelength $4\pi h_s$, and it is less surface-intensified than the Stokes drift of a realistic wave spectrum (Webb & Fox-Kemper 2011). The sign of the adjustment fields would switch with a change in the sign of v_s and S_s. This formula implies that in defining ϵ we choose the Stokes velocity scale V_s in (3.3) as equal to the surface value of the along-axis component of Stokes drift v_s. As remarked just above (2.6), the cross-axis Stokes component u_s simply induces an anti-Stokes flow u during the adjustment. If the gravity wave field is perpendicular to the initial flow, then the associated vortex force is zero; the Stokes Coriolis force is cancelled by the anti-Stokes flow $u' = -u_s$; and $v' = b' = 0$ after the adjustment, hence $v = v_0$ and $b = b_0$.

A frontal solution is shown in figure 3 for $\mathscr{B} = 1$ and $\lambda = 2$ and constant stratification ($N^2 = 1$). The adjustment in b' is a positive monopole centred on the

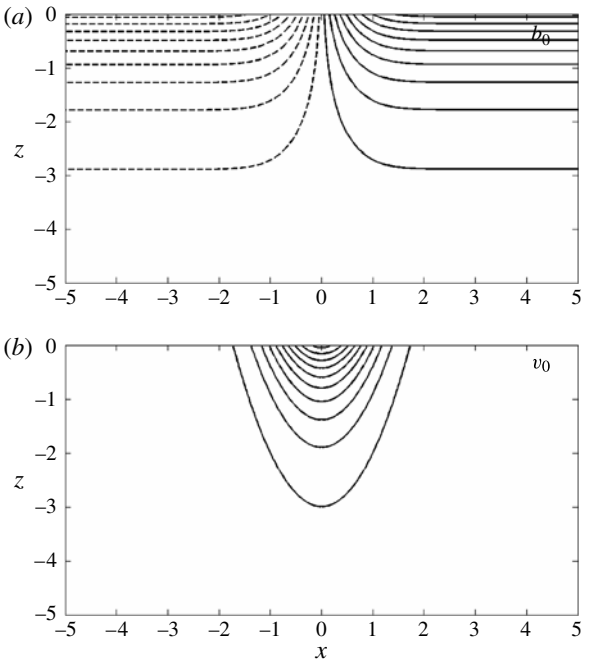

FIGURE 2. Initial frontal fields $b_0(x, z)$ and $v_0(x, z)$ from (4.8). The contours have an interval of 0.1 and straddle zero. Positive and negative contours are solid and dashed, respectively.

front at a depth of the base of the Stokes flow layer, $z \approx -\lambda^{-1}$. Its shape is broadly like that of v_0 except that b' vanishes toward the surface to satisfy the boundary condition. The accompanying v' has subsurface extrema at a similar depth, but it is a negative (up-front) flow on the light side of the front ($x > 0$) and positive (down-front) flow on the dense side, with weak opposing flows in a very thin layer closer to the centre of the front. When added to the initial front (v_0, b_0), the adjustment has the effect of shifting the centre of the front leftward toward the dense side beneath the surface, in association with the Stokes flow that has a positive along-front component. Because waves often are aligned with winds, the leading-order cross-front shift has the curious effect that it opposes the Ekman overturning circulation driven by down-front winds (Thomas 2005). Thus, conservative wave adjustment may act to destabilize the front when the wind tends to stabilize it, and stabilize it when the wind tends to destabilize.

The adjustment displacement field has an anti-symmetric χ', with convergent inward displacements within the Stokes flow layer coming from the sides; downward displacements in the centre; and divergent (outward and downward) displacements at depth. Because of the even horizontal symmetry in b' for a front, $\chi'_0 = 0$ from (4.3). In the horizontal far field, $\chi'(z)$ and $\xi'(z) \neq 0$, but they are horizontally uniform and have opposite sign on the two sides, with no net horizontal displacement across the front. The sense of v' is consistent with a Coriolis torque, $\partial_z v'$, forced by the frontal torque, $-S_s \partial_x v_0$, associated with the cross-front Stokes vortex force in the the first equation in (3.4). The buoyancy torque, $-\partial_x b'$, partly opposes the v' flow response, but not to the full extent of thermal wind balance. Below the Stokes flow layer, the forcing term in (4.5) becomes very small, and thermal wind balance holds. However,

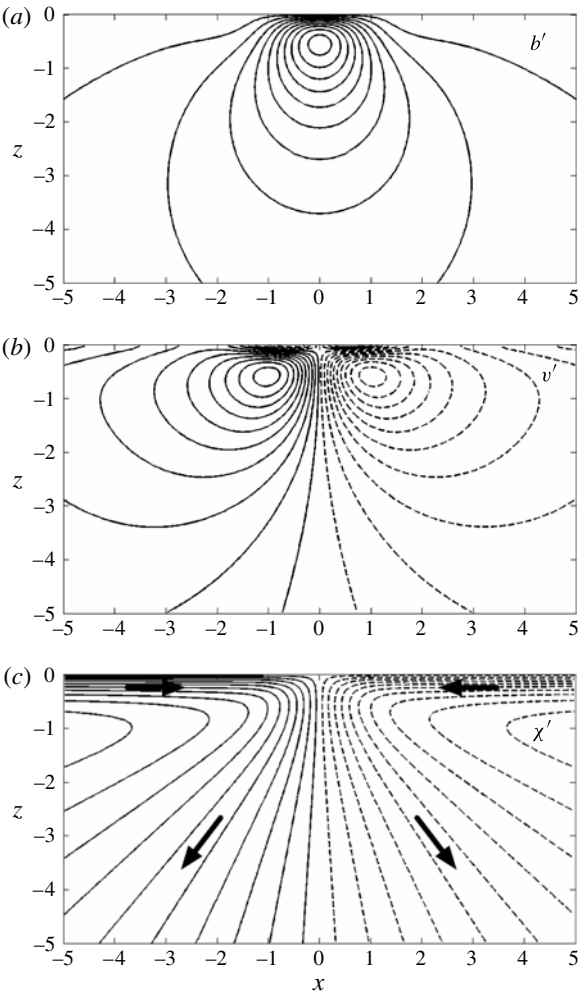

FIGURE 3. Wave-adjustment fields for the front (4.8) with $\mathscr{B} = 1$ and $\lambda = 2$ and constant N: (*a*) $b'(x, z)$; (*b*) $v'(x, z)$; (*c*) $\chi'(x, z)$. The fields are normalized by their extreme magnitudes (i.e. 0.21, 0.12, and 0.25, respectively) and contoured with an interval of 0.1 straddling zero. Positive and negative contours are solid and dashed, respectively. The along-front Stokes drift is directed toward positive y. All signs reverse if the along-front Stokes drift is reversed.

the wave-adjusted buoyancy peaks near $z = 1/\lambda$, and it decays slowly below, as does the wave-adjusted velocity. The pattern in b' relates to the vertical displacement ζ' as buoyancy conservation of the mean stratification $\overline{b}(z)$, as expressed in (4.1); the displacement contributions from $b_0(x, z)$ would arise at $O(\mathscr{R})$.

Where the right-side forcing is small, the homogeneous b' and v' solutions of the left-side elliptic operator (4.5) that decay to zero in the far field have the form of r^{-n} times either $\cos[n\theta]$ or $\sin[n\theta]$, where r and θ are cylindrical coordinates in the $(x, \mathscr{B}^{1/2}z)$ plane. For the frontal flow, as can be derived by expanding the logarithmic argument in (4.7) for large r, the leading-order solutions vary as the $n = 1$ solution,

$$b' \sim \frac{\sin[\theta]}{r} = \frac{\mathscr{B}^{1/2}z}{r^2}, \quad v' \sim \frac{\cos[\theta]}{r} = \frac{x}{r^2}. \tag{4.10}$$

This indicates a long reach, $\sim 1/r$, in the frontal adjustment fields even though the Stokes drift forcing decays exponentially faster.

The patterns in the wave adjustment fields are essentially invariant across parameter changes in $\mathscr{B}$ and λ, though their amplitudes and scales do change. Here we summarize these dependences qualitatively, and then do so more explicitly with the semi-separable approximation in § 4.3. For different $\mathscr{B}$ values and fixed λ (not shown), the wave adjustment process behaves similarly to the familiar geostrophic adjustment process in response to an initially unbalanced state (McWilliams 2006). For small $\mathscr{B}$ (i.e. a front wider than deformation radius, $\ell > \mathscr{N}h/f$ in dimensional quantities), the adjustment patterns are similar to figure 3, but they extend deeper in z while contracting slightly in x. As $\mathscr{B}$ decreases, the velocity adjustment v' magnitude is larger, while the buoyancy adjustment b' magnitude changes only slightly. That is, the wave-induced adjustment tends to make the final frontal structure have a larger effective $\mathscr{B}$ value, closer to unity. For large $\mathscr{B}$, the opposite happens: the adjustment fields have a slightly larger x scale, smaller z scale, bigger b', and similar v', indicating a decrease in the effective $\mathscr{B}$ value of the front after adjustment. Thus, the width of the wave-adjusted front is closer to the upper-ocean deformation radius than is the initial front. For different λ values and fixed $\mathscr{B}$ (also not shown), the subsurface extrema shift vertically according to the scale λ^{-1}, and the amplitudes of b' and v' decrease as λ increases (due to the lesser vertical extent of $\mathscr{F}'$ in the $\tilde{z}$ integration in (4.7)).

4.1.2. *Filament*

We define a simple initial cold filamentary flow and buoyancy anomaly by

$$v_0(x,z) = c_0 x \mathrm{e}^{-x^2+z}, \quad b_0(x,z) = -\frac{c_0}{2}\mathrm{e}^{-x^2+z}. \tag{4.11}$$

This is a negative b_0 anomaly at the surface, with a pair of opposite jets on either side (figure 4). With $c_0 = \sqrt{2}\mathrm{e}^{0.5} = 2.33$, the maximum velocity is equal to one at $(1/\sqrt{2}, 0)$, and the minimum in b_0 is -1.17 at $(0,0)$; v_0 is odd in x, and b_0 is even. With this symmetry the evaluation of (4.7) can be shortened by restricting the $\tilde{x}$ integration to the positive half-line and replacing the logarithmic argument with $r^2(\tilde{x},\tilde{z})r^2(-\tilde{x},-\tilde{z})r^2(\tilde{x},-\tilde{z})r^2(-\tilde{x},\tilde{z})$. We use the same Stokes profile (4.9).

The adjustment fields have very different shapes for a filament (figure 5). Again b', v', and χ' have subsurface extrema at the base of the Stokes flow layer, in the sense of Coriolis torque balancing vortex-force torque. Here v' is primarily a positive monopole centred on the filament with weak negative lobes on each side, while b' is a dipole that is lighter on the right side and denser on the left side. The overall shape of b' is topologically similar to v_0 except for weakening to zero at the surface. When added to the primary filament fields, these adjustment fields have the effect of moving the subsurface centre of the filament to the left in x. The displacement field χ' is a clockwise movement around the filament, rightward within the Stokes flow layer and leftward in a deep layer underneath. Once again, this displacement pattern opposes the sense of the Ekman buoyancy flux overturning, if winds were aligned with the waves. The localization condition (4.3) gives $\chi_0'(z) \neq 0$ because b' is odd symmetric about $x = 0$ in a filament, and this implies that $\chi', \xi' \to 0$ as $x \to \pm\infty$. In all the fields, the filamentary far-field adjustment is more confined than for a front, with a

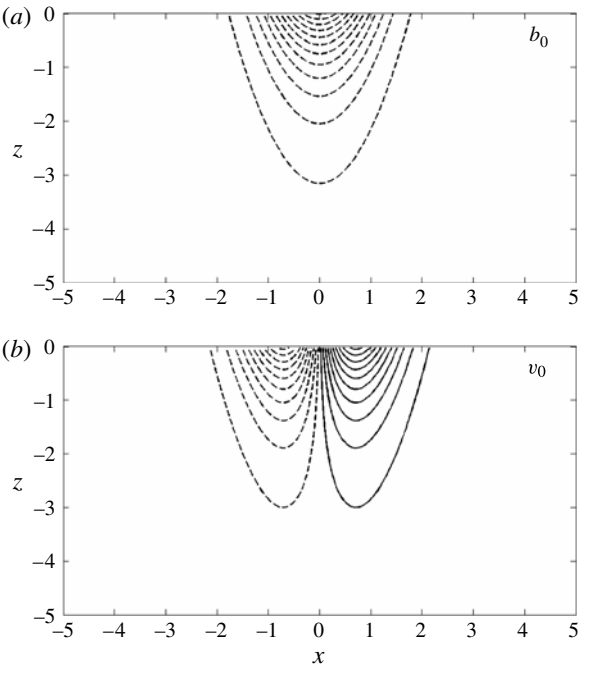

FIGURE 4. Initial cold filamentary fields $b_0(x, z)$ and $v_0(x, z)$ from (4.11). The contours have an interval of 0.1 and straddle zero. Positive and negative contours are solid and dashed, respectively.

dominant $n = 2$ structure of

$$b' \sim \frac{\sin[2\theta]}{r^2} = \frac{2\mathscr{B}^{1/2}xz}{r^4}, \quad v' \sim \frac{\cos[2\theta]}{r} = \frac{x^2 - \mathscr{B}z^2}{r^4}, \tag{4.12}$$

i.e. $\sim 1/r^2$ as $r \to \infty$. Even so, the decay is much slower than the decay of S_s or the initial filament fields. The $\mathscr{B}$ and λ dependences for the filament are similar to those for the front (see also § 4.3).

4.2. *Variable* $N^2(z)$

We choose canonical upper-ocean stratification as a simple, monotonic profile for a nearly mixed layer above a broad pycnocline:

$$N^2(z) = \mathscr{B}_m + \frac{\mathscr{B} - \mathscr{B}_m}{2}(1 - \tanh[\lambda_m(z + h_m)]). \tag{4.13}$$

Within the mixed layer, $N^2 \approx \mathscr{B}_m$, and at depth $N^2 \to \mathscr{B}$. For a mixed layer above a sharp transition to the pycnocline at $z \approx -h_m$, we take $0 \leqslant \mathscr{B}_m \ll \mathscr{B}$ and $\lambda_m h_m \gg 1$ for a sharp transition between the mixed layer and pycnocline.

The PDE system (3.4) and its boundary conditions are solved numerically in the limit of $\epsilon\mathscr{R} \to 0$ by expanding in Chebyshev basis functions algebraically mapped from $x' \in [-1, 1]$ to $x \in [-\infty, \infty]$ using basis functions $TB_n(x)$ and from $z' \in [-1, 1]$ to $z \in [-\infty, 0]$ using $TL_n(z)$, as laid out by Boyd (2000). A similar infinite half-plane approach was used for atmospheric linear instability calculations by Lin & Pierrehumbert (1988). This representation is well suited to localized

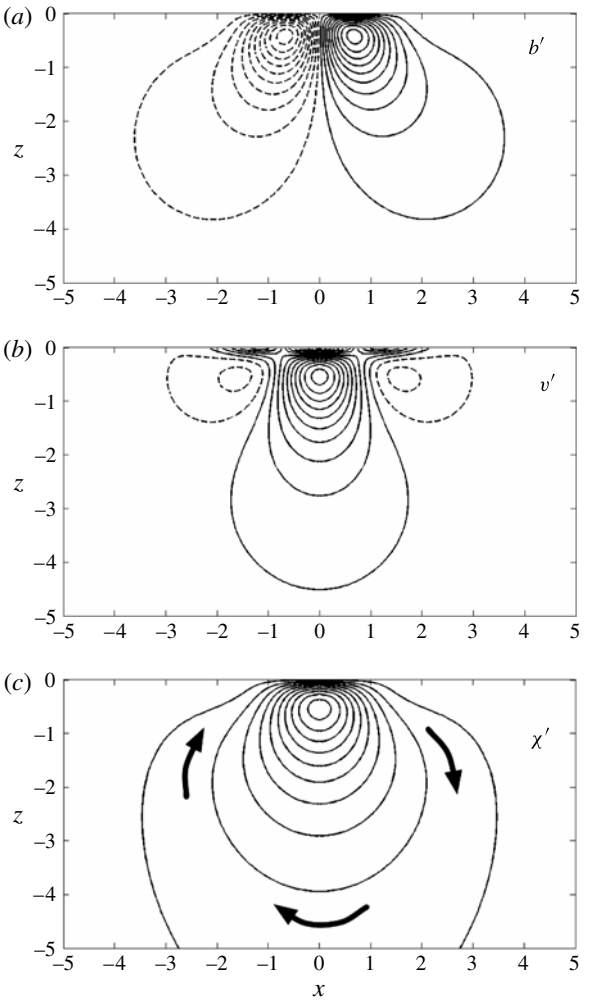

FIGURE 5. Wave-adjustment fields for the cold filament (4.11) with $\mathscr{B} = 1$ and $\lambda = 2$ and constant N: (*a*) $b'(x, z)$; (*b*) $v'(x, z)$; (*c*) $\chi'(x, z)$. The fields are normalized by their extreme magnitudes (i.e. 0.21, 0.24, and 0.24, respectively) and contoured with interval of 0.1 straddling zero. Positive and negative contours are solid and dashed, respectively, when the along-filament Stokes drift is directed toward positive y.

functions that vanish in the far field. The mapping functions are $x = L_x x'/\sqrt{1 - x'^2}$ and $z = -L_z(1 + z')/(1 - z')$ and the collocation points are at $x'_i = \cos(\pi i/M)$ and $z'_j = \cos(\pi j/N)$, with their respective truncation numbers of M and N ranging from 30 to 60 depending on the parameter choices. Results presented here are qualitatively robust to doubling the truncation numbers and varying the mapping function coefficients ($L_x = 2$, $L_z = 4$) by a factor of 3. The primary advantages to this approach are: (i) spectral accuracy in differentiation; (ii) high collocation resolution near the upper boundary where the Stokes drift varies rapidly; (iii) high collocation resolution near the centre of the front or filament feature; and (iv) bounded behaviour at infinity. The stratification $N^2(z)$ and the pseudo-spectral collocation of right-side 'forcing' terms are evaluated on the Gauss–Lobatto 'endpoints' grid. Some care is

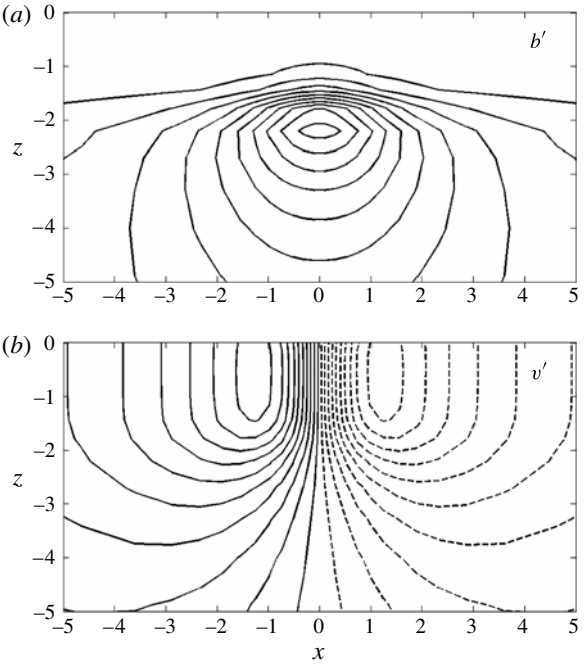

FIGURE 6. Wave-adjustment fields for the front (4.8) with $\lambda = 2$ and a mixed layer $N(z)$ from (4.13) with $\mathscr{B}_m = 0.01, h_m = 1.7$, and $\lambda_m = 3$ at leading order in $(\epsilon, \mathscr{R})$: (*a*) $b'(x, z)$; (*b*) $v'(x, z)$. The fields are normalized by their extreme magnitudes (i.e. 9.1 and 7.1, respectively) and contoured with an interval of 0.1 straddling zero. Positive and negative contours are solid and dashed, respectively, when the along-filament Stokes drift is directed toward positive y.

required in evaluating first-order relations, such as (4.6), because two endpoints in x are located at infinity. For this reason, first-order equation solutions must be performed in (x', z') and then transformed to (x, z) by a change of variables. The method in § 5 employs the same rescaled coordinates using an iterative method when $\epsilon \neq 0$.

Frontal and filamentary adjustment solutions to the leading-order approximation to (3.4) with variable $N(z)$ show a remarkable degree of pattern similarity to the constant-N solutions in § 4.1, even across a wide range of the stratification profile parameters in (4.13). $N^2(z)$ deforms and modulates the adjustment patterns but essentially does not change their gross shape; e.g. $b'(x, z)$ is a positive, subsurface monopole for a front with either a uniform or mixed-layer stratification profile. In general terms, a small mixed-layer value of $\mathscr{B}_m$ widens and deepens the adjustment response, analogous to the overall $\mathscr{B}$ dependence for constant N. This is a modest effect for $h_m < 1$ (a shallow mixed layer compared to frontal depth scale), but it becomes quite strong for $h_m > 1$ and $\mathscr{B}_m \ll 1$, i.e. fronts shallower than the mixed layer but wider than the mixed layer deformation radius. The perturbation fields (b', v') are wider with a mixed layer (figures 6–7) than with the interior stratification uniform up to the surface (figures 3 and 5). In both fronts and filaments, $v'(x, z)$ is strong with weak vertical shear all across the mixed layer, and $b'(x, z)$ amplifies from zero at the surface to a strong response within the transition zone between the mixed layer and pycnocline (figures 6 and 7 for $\mathscr{B}_m = 0.01$ and $h_m = 1.7$). In an initial value problem, where waves arrive at a front suddenly and then adjustment follows over the next inertial periods, this

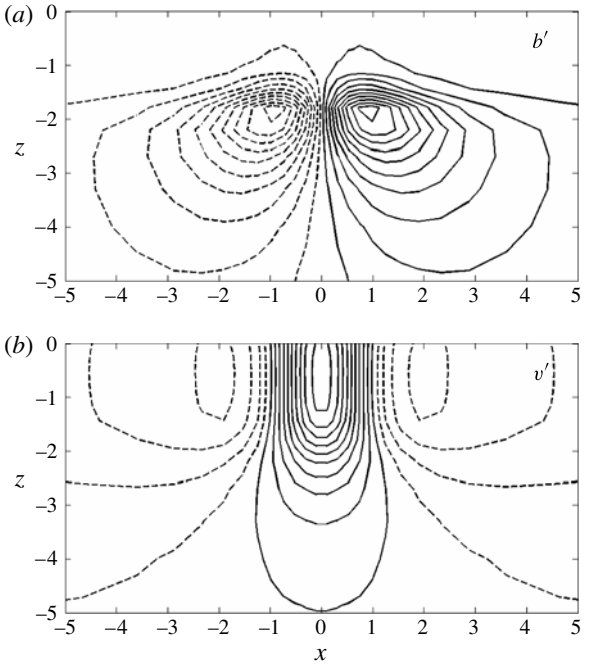

FIGURE 7. Wave-adjustment fields for the cold filament (4.11) with $\lambda = 2$ and a mixed layer $N(z)$ from (4.13) with $\mathscr{B}_m = 0.01$, $h_m = 1.7$, and $\lambda_m = 3$ at leading order in $(\epsilon, \mathscr{R})$: (*a*) $b'(x, z)$; (*b*) $v'(x, z)$. The fields are normalized by their extreme magnitudes (i.e. 4.6 and 10.4, respectively) and contoured with an interval of 0.1 straddling zero. Positive and negative contours are solid and dashed, respectively, when the along-filament Stokes drift is directed toward positive y.

buoyancy perturbation is likely to generate very strong internal waves radiating along the mixed layer base. The adjusted-state displacement fields (not shown) are quite similar in shape to the constant-N solutions (§ 4.1) in spite of the deep mixed layer. With these particular parameter values, the adjustment amplitudes are nearly 100 times stronger than without a mixed layer (cf. figures 3 and 5 for $\mathscr{B}_m = \mathscr{B} = 1$).

4.3. *Semi-separable approximation*

In this subsection we provide an approximate explanation and parameter analysis of the wave-adjustment amplification with $N(z)$ demonstrated in § 4.2. Readers more interested in the rigorous solutions of the adjustment problem may skip ahead to § 5.

The leading-order, linear system (3.4) with zero right sides does not have exactly (x, z)-separable solutions even when the forcing terms are separable (as with the profiles (4.8), (4.9) and (4.11)). But they are close to having separable solutions, and we can obtain useful approximate solutions that we call semi-separable. Their utility is as a simpler explanation of the frontal and filamentary solutions above.

For the frontal case with the S_s, v_0 and b_0 profiles above, we define two-dimensional b', $v'(x, z)$ solution forms by

$$b' \approx \tilde{b}(z)\, \mathrm{e}^{-x^2}, \quad v' \approx \tilde{v}(z)\, (-2x\mathrm{e}^{-x^2}). \tag{4.14}$$

We substitute these into (3.4) and delete terms proportional to $x^2 \exp[-x^2]$, i.e. we make an approximation based on small x to obtain a one-dimensional system

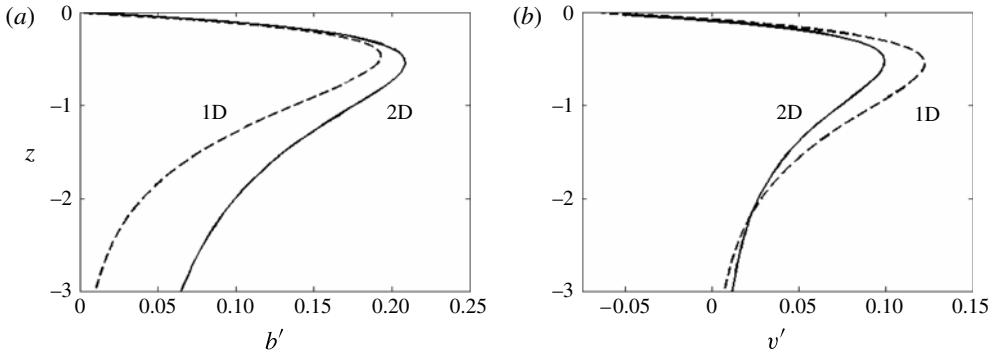

FIGURE 8. A comparison of frontal wave-adjustment profiles for a front with $\mathscr{B} = 1$ and $\lambda = 2$ and constant N (cf. figure 3): the one-dimensional (1D) semi-separable profiles, $\tilde{b}(z)$ (*a*) and $\tilde{v}(z)$ (*b*), and their two-dimensional (2D) counterparts, $b'(0, z)$ and $\lim_{x\to 0}[v'(x, z)/(-2x)]$, as determined from (4.14).

for $\tilde{b}$, $\tilde{v}(z)$,

$$\left[\partial_z^2\left(\frac{1}{N^2}\right) - 2\right]\tilde{b} = -2\mathrm{e}^{(1+\lambda)z} - \partial_z\left(\frac{\mathrm{e}^{(1+\lambda)z}}{N^2}\right), \tag{4.15a}$$

$$\tilde{v} = \frac{1}{2}\left(\partial_z\left(\frac{\tilde{b}}{N^2}\right) + \frac{\mathrm{e}^{(1+\lambda)z}}{N^2}\right), \tag{4.15b}$$

with boundary conditions $\tilde{b}(0) = 0$ and vanishing amplitudes as $z \to -\infty$.

For constant buoyancy frequency, $N(z) = \mathscr{B}$, we have closed-form analytic solutions to (4.15):

$$\tilde{b}(z) = \frac{1 + \lambda + 2\mathscr{B}}{(1+\lambda)^2 - 2\mathscr{B}}\left(\mathrm{e}^{\sqrt{2\mathscr{B}}z} - \mathrm{e}^{(1+\lambda)z}\right), \tag{4.16a}$$

$$\tilde{v}(z) = \frac{1 + \lambda + 2\mathscr{B}}{\sqrt{2\mathscr{B}}((1+\lambda)^2 - 2\mathscr{B})}\mathrm{e}^{\sqrt{2\mathscr{B}}z} - \frac{2 + \lambda}{(1+\lambda)^2 - 2\mathscr{B}}\mathrm{e}^{(1+\lambda)z}. \tag{4.16b}$$

Both fields exhibit two vertical decay rates: $1 + \lambda$ associated with the frontal and Stokes flows and $\sqrt{2\mathscr{B}}$ associated with the vertical stratification. These show the contraction of the vertical scale of the adjustment for a shallower Stokes profile (larger λ) and a stronger stratification (larger $\mathscr{B}$), and *vice versa*, as described in § 4.1.1. Here $\tilde{b}(z)$ is always positive and convex in shape with a subsurface maximum; $\tilde{v}(z)$ is usually negative at the surface (note that this occurs in the thin surface layer of reverse flow in figure 3) except when $\mathscr{B} < 0.5$, but $\tilde{v}(z)$ is always positive at depth, so $\tilde{v}$ too has a subsurface maximum. (Note that the zero of the denominators in (4.16) at $\sqrt{2\mathscr{B}} = \lambda + 1$ is not a singularity.)

How accurate is the semi-separable solution? We assess it compared to the complete solution (4.7) in figure 8 at the centre of the front. It is very accurate near the surface, and it is reasonably accurate, within 10 % or so, down through the peaks in b' and z' near the base of the frontal flow. However, it becomes inaccurate at depth, with algebraic decay in z in the complete solution (4.10) and exponential decay in the semi-separable one (4.16). This is a consequence of the non-locality in the elliptical boundary-value problem (4.5) and its Green's function solution (4.7): in the upper

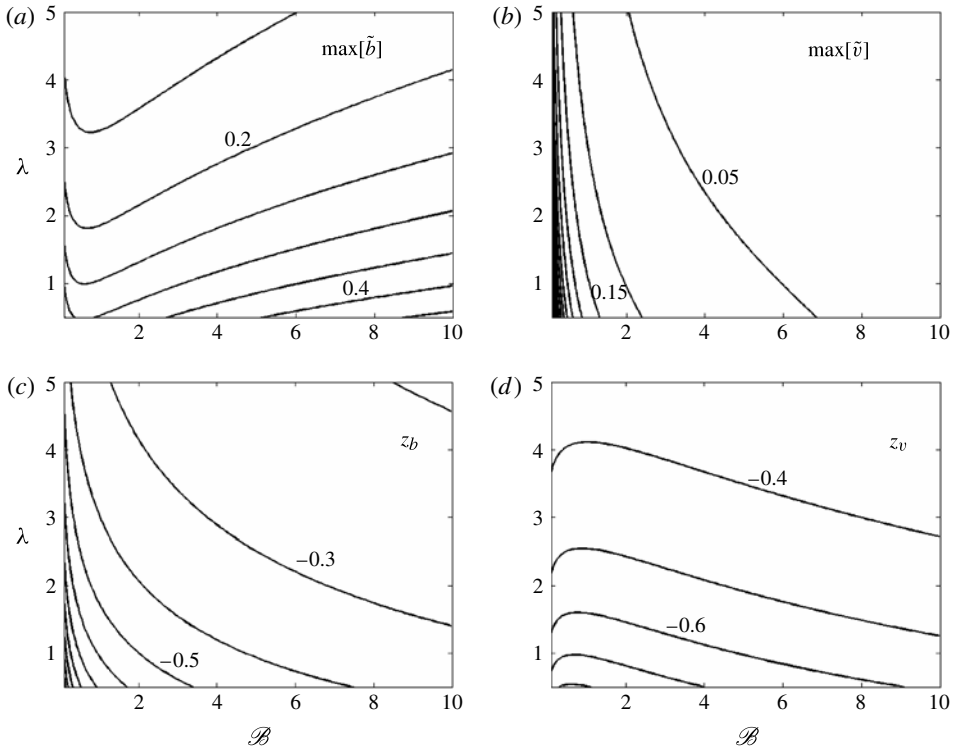

FIGURE 9. Vertical profile maxima for the semi-separable frontal adjustment solutions (4.16) with constant N. Top row: max[$\tilde{b}$] (*a*) and max[$\tilde{v}$] (*b*). For both maxima the contour interval is 0.05. Bottom row: positions of the maxima, z_b (*c*) and z_v (*d*). The contour interval is 0.1.

region for $b'(x, z)$ with small x, the important contributions from the forcing integrand, $\mathscr{F}'(\tilde{x}, \tilde{z})$, are ones with small r associated with small $\tilde{x}$, so the approximation is accurate, whereas at depth, both small and intermediate values of $\tilde{x}$ have very nearly the same r values, and the small $\tilde{x}$ approximation is not accurate. Similarly, the far field in x is inaccurately approximated in the semi-separable model. However, the larger adjustment amplitudes are in the upper regions not far from the front centre, and thus the accuracy of $\tilde{b}(z)$ and $\tilde{v}(z)$ is sufficient to explain these primary features of $b'(x, z)$ and $v'(x, z)$.

The parameter dependences of the subsurface maxima implied by the semi-separable solution (4.16) for constant N are graphically demonstrated in figure 9. Here $\tilde{b}$ is larger for larger $\mathscr{B}$ and smaller λ, except for a small increase as $\mathscr{B} \to 0$; $\tilde{v}$ increases as $\mathscr{B}$ decreases, with a much weaker dependence on λ. The depths of the maxima, z_b and z_v respectively, mostly decrease with increasing $\mathscr{B}$ and λ. Both adjustment amplitudes decrease $\sim 1/\lambda$ for large λ; however, recall from (3.3) that the prefactor ϵ is $\propto \lambda$, so in this limit the non-dimensional wave adjustment amplitudes vary as $\epsilon(b', v') \sim \mu\mathscr{R}$, independent of λ. This shows that even a very shallow Stokes shear profile still has an adjustment effect $\propto \mu = La^{-2}$, the Stokes drift amplitude.

For the most part, all of these adjustment properties vary within moderate ranges. An exception is for small $\mathscr{B}$ where $\tilde{v}(z)$ becomes very large and slowly decays

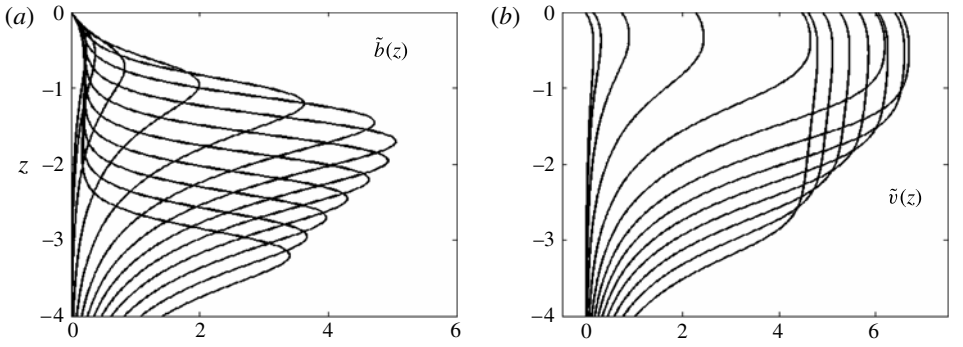

FIGURE 10. Vertical profiles of the semi-separable, frontal-adjustment response $\tilde{b}(z)$ and $\tilde{v}(z)$ from (4.15) with a mixed layer $N(z)$ from (4.13) with $\mathscr{B}_m = 0.01$, $\lambda_m = 3$, and h_m values ranging from 0 to 3 in increments of 0.25 with successively deeper response profiles. In this set the largest amplitudes occur at $h_m = 1.5$.

with depth. Here we can further approximate (4.16) by

$$\tilde{b}(z) \approx \frac{\mathrm{e}^{\sqrt{2\mathscr{B}}z}}{1+\lambda}, \quad \tilde{v}(z) \approx \frac{\mathrm{e}^{\sqrt{2\mathscr{B}}z}}{\sqrt{2\mathscr{B}}(1+\lambda)}, \tag{4.17}$$

except within a small distance $\sim(1+\lambda)^{-1}$ of the surface; $\tilde{v}$ grows without limit as the stratification weakens ($\mathscr{B} \to 0$), even though the amplitude of $\tilde{b}$ remains bounded. The static stability constraint (3.11) implies a lower limit on $\mathscr{B}$ that precludes taking the limit $N^2 \to 0$ for a fixed $\mathscr{R} > 0$. This constraint is likely to be most severe in the mixed layer where N^2 is smallest. Nevertheless, the depths of the subsurface maxima, derived from the full solution (4.16), remain fairly close to the surface. The depth of the velocity maximum varies as $z_v \to -\ln[2+\lambda]/(1+\lambda) < 0$, which is independent of $\mathscr{B}$ as $\mathscr{B} \to 0$. The depth of the buoyancy maximum varies as $z_b \to \ln[\mathscr{B}]/2(1+\lambda) < 0$, which is only weakly deepening in this small-$\mathscr{B}$ limit.

For a uniformly stratified ocean, weak stratification does not usually occur where fronts and filaments arise, so the preceding limit is not very realistic. However, fronts and filaments are common in the presence of a weakly stratified mixed layer above a pycnocline, as represented in the $N(z)$ profile (4.13), and we have seen that this situation has a large and deep adjustment response (figures 3–5). To understand this, we use the simplified semi-separable approximation (4.15), although now no explicit analytic solutions are known for $\tilde{b}(z)$ and $\tilde{v}(z)$, so the solution procedure is numerical. It is solved with second-order finite differences integrated upward in z from below. We add together the inhomogeneous solution that vanishes in the far field plus a multiple of the homogeneous solution with far-field decay $\propto \exp[\sqrt{2\mathscr{B}}z]$ to satisfy the surface boundary condition, $\tilde{b}(0) = 0$. We again confirm approximate accuracy compared to the complete leading-order solution of (3.4) near the frontal centre and in the depth ranges around and above the subsurface maxima in b' and v' (similar to figure 8).

With a mixed layer $N(z)$, the adjustment responses in both $\tilde{b}$ and $\tilde{z}$ increase significantly with increasing h_m up to a value somewhat larger than the frontal depth (non-dimensionally equal to 1); in figure 10 the maximum response is at $h_m = 1.5$. With further increases in h_m, the response amplitudes slowly decrease although their vertical extent continues to deepen up to the point with $h_m \approx 1/\sqrt{2B_m} \gg 1$ where the

mixed layer looks uniformly stratified, as in (4.17). A prescription for this 'sweet spot' value in h_m comes from a vertical integral of the second relation in (4.15):

$$\int_{-\infty}^{0} \mathrm{d}z\tilde{v} = \frac{1}{2}\int_{-\infty}^{0} \mathrm{d}z\frac{\mathrm{e}^{(1+\lambda)z}}{N^2(z)}, \tag{4.18}$$

using the zero boundary conditions on $\tilde{b}$. For small $\mathscr{B}_m$ and h_m neither very large nor very small, $\tilde{v}(z)$ has the 'mixed layer' structure evident in figures 6, 7 and 10, *viz.* a nearly uniform amplitude $\approx\tilde{v}_m$ for $z > -h_m$ and decaying $\sim\mathrm{e}^{\sqrt{2\mathscr{B}}z}$ underneath. This structural approximation to $\tilde{v}(z)$ is easily integrated for the left side of (4.18), yielding a depth factor of $h_m + 1/\sqrt{2\mathscr{B}}$ that can be divided through to obtain

$$\tilde{v}_m \approx \frac{1}{2h_m + \sqrt{2/\mathscr{B}}}\int_{-\infty}^{0} \mathrm{d}z\frac{\mathrm{e}^{(1+\lambda)z}}{N^2(z)}, \tag{4.19}$$

which is fully specified in terms of the stratification function (4.13) and parameters $\mathscr{B}$, $\mathscr{B}_m$, λ, λ_m, and h_m. In particular, for large h_m, we can approximate (4.19) by assuming $N^2(z) \approx \mathscr{B}_m$ in the integral, to obtain the explicit formula

$$\tilde{v}_m \approx \frac{1}{2h_m + \sqrt{2/\mathscr{B}}}\frac{1}{(1+\lambda)\mathscr{B}_m}. \tag{4.20}$$

This approximate formula agrees well with the large-h_m end of the curve plotted in figure 11.

Indeed, $\tilde{v}_m$ does have a sweet spot in h_m, which we define as $\tilde{v}_* = \max_{z,h_m}[\tilde{v}(z,h_m)]$. In figure 11, $\tilde{v}_m(h_m)$ has a rather broad peak in h_m around an order-one value, here $h_* = 1.5$. The asymptotic scaling of $\tilde{v}_m$ is $\sim 1/\sqrt{\mathscr{B}_m}$ for large h_m and small $\mathscr{B}_m$. The right side of (4.19) scales as $\sim 1/(h_m\mathscr{B}_m)$, which is consistent with the constant-N solution (4.17) for $h_m \sim 1/\sqrt{\mathscr{B}_m}$. Thus, the sweet spot response with order-one h_m is much stronger than can be explained just by the weakness of the stratification alone. The sweet-spot amplitude $\tilde{v}_*$ is most strongly a function of the mixed-layer stratification, with $\tilde{v}_* \sim 1/\mathscr{B}_m$, which grows without limit as the stratification vanishes. The sweet spot is a more modest function of the other parameters in the most common oceanic regime: h_* and $\tilde{v}_*$ decrease as $\lambda > 1$ increases; h_* decreases and $\tilde{v}_*$ increases slightly as $\lambda_m > 1$ increases; and h_* and $\tilde{v}_*$ both decrease as $\mathscr{B} \sim 1$ increases.

Around the sweet spot, $\tilde{b}(z)$ is much weaker than $\tilde{v}(z)$ within the mixed layer (figures 6, 7 and 10). It is smaller by a factor $\sim\sqrt{2\mathscr{B}_m} \ll 1$, consistent with the homogeneous solution component in a uniform stratification $N^2 = \mathscr{B}_m$ (see (4.16)). Entering into the pycnocline, however, $\tilde{b}(z)$ grows rapidly to approximately match v_m because of thermal wind balance beneath the frontal and Stokes flows; i.e. $\partial_x b' \approx \partial_z v'$ or $\tilde{b} \approx \partial_z\tilde{v} \approx \sqrt{2\mathscr{B}}v_m \sim v_m$.

In the leading-order adjustment model, a filament has the opposite x-symmetry to a front. It too can be analysed in a semi-separable approximation, in this case with $b' \propto x\mathrm{e}^{-x^2}$ and $v' \propto \mathrm{e}^{-x^2}$ near the centre (see the patterns in figures 5 and 7). The resulting adjustment response equations have the same functional form as (4.15) with only a difference in the coefficients. So all the qualitative conclusions about parameter dependences and vertical structure are essentially the same for both filaments and fronts.

In the asymptotic ordering of the wave-balanced fields (3.2), the perturbation fields were seen to be $O(\epsilon)$ compared to the initial fields. Section 1 and figure 1 indicate that this parameter is often larger than the Rossby number, so wave adjustment may

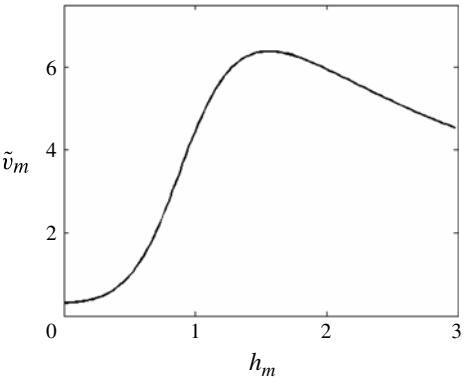

FIGURE 11. The wave-adjustment velocity amplitude $\tilde{v}_m$ from (4.13), (4.15), or approximately from (4.19), as a function of mixed layer depth h_m for a front with $\lambda = 2$, $\mathscr{B} = 1$, $\mathscr{B}_m = 0.01$, and $\lambda_m = 3$. The maximum is defined as $\tilde{v}_*$ at h_*.

be important even when $\mathscr{R}$ is small. The preceding sections show that the perturbation field accompanying this scale factor varies substantially with the stratification. In the constant stratification cases shown, the peak in b' is $O(0.2)$, substantially reducing the magnitude of the wave adjustment. However, in the sweet-spot examples with variable $N^2(z)$, the perturbation fields peak near $O(5)$ in locations somewhat remote from the v_0 flow. These assessments were made by neglecting the right-hand sides of (3.4), yet they seem robust for determining magnitudes of the response. The next section shows that considering $\epsilon \sim 1, \mathscr{R} \ll 1$ changes the shape but minimally impacts the magnitude of the wave adjustment responses.

5. Finite-ϵ wave adjustment

As remarked in § 3, we can solve (3.4)–(3.5) by iteration with an expectation of convergence for small enough ϵ and $\mathscr{R}$. Rather than do so generally, we focus on a particular limit of $\mathscr{R} \ll \epsilon \lesssim 1$. This is the expected oceanic regime for nearly geostrophic fronts with strong surface waves, $\mu\lambda \gg 1$, and it is empirically supported by figure 1. This greatly simplifies the general solution procedure and provides an indication of the effects of finite ϵ. While ϵ is a formal ordering parameter in (3.2)–(3.3), it does not appear explicitly in the leading-order model (§ 4), and it should be understood here as representative of the relative size of the wave-induced adjustment fields. In the case of large non-dimensional adjustment amplitude (e.g. near a sweet spot; figures 6–7), the effective size of the wave-induced correction is larger than the formal estimate of ϵ.

In the limit $\mathscr{R} \ll \epsilon \lesssim 1$, we neglect all higher-order corrections in $\mathscr{R}$ while retaining terms proportional to ϵ. Thus, the static stability constraint (3.11) is again assured asymptotically by $\mathscr{R} \ll 1$. In the right sides (3.5) of the system (3.4), neglecting $O(\mathscr{R})$ terms leaves only the following correction effects to the leading-order adjustment:

$$\epsilon \mathscr{P}' = -\epsilon S_s \partial_x v', \quad \epsilon \mathscr{Q}' \approx -\epsilon S_s \partial_x b', \quad \mathscr{R}\mathscr{T}' \approx \epsilon \mathscr{R}\mathscr{W}' \approx 0. \tag{5.1}$$

These terms in $\mathscr{P}'$ and $\mathscr{Q}'$ represent the vortex force due to the wave adjustment fields. We retain these corrections while otherwise following the derivation path in § 4.

The generalization of the elliptic boundary-value problem (4.5) for b' is

$$\partial_x^2 b' + \partial_z^2 \left(\frac{b'}{N^2} \right) = \mathscr{F}' + \partial_z \left(\frac{\epsilon \mathscr{Q}'}{N^2} \right) - \partial_x \epsilon \mathscr{P}'$$
$$= \mathscr{F}' - \epsilon \left(\frac{S_s^2}{N^2} \partial_x \partial_z v_0 + 2 S_s \partial_z \left(\frac{\partial_x b'}{N^2} \right) + (\partial_z S_s) \left(\frac{\partial_x b'}{N^2} \right) + \epsilon S_s^2 \left(\frac{\partial_x^2 b'}{N^2} \right) \right), \quad (5.2)$$

with homogeneous boundary conditions for b' because $\mathscr{T}'(x, 0) \approx 0$ in (3.10). This is a linear system for b', which could in principle be solved directly. Instead, we solve it iteratively as $Lb'^n = R[b'^{n-1}; \epsilon], n = 2, 3, \ldots,$ starting with $b'^1 = 0$. Iteration convergence is aided for finite ϵ by additionally incrementing the value of $\epsilon^k = k\Delta\epsilon$ in the right-side evaluation, for $k = 1, \ldots, K$ and $\Delta\epsilon = \epsilon/K$. For larger values of ϵ, convergence is further aided by relaxation at each iterative step; i.e. $b'^n \leftarrow (1 - \alpha) b'^n + \alpha b'^{n-1}$ for $\alpha > 0$. For very large values of ϵ, the iteration does not converge. An advantage of iteration is that the same elliptic solvers in §§ 4.1 and 4.2 can be applied to the inversion of L. As before, we consider $S_s > 0$, but in this case the sign symmetry with respect to S_s is more complicated because the right-hand side of (5.2) is nonlinear in Stokes shear. The finite-ϵ sign symmetry is $(x, z, \gamma, b', v', v_0, S_s) \leftrightarrow (-x, z, \gamma, -b', v', v_0, -S_s)$, where γ is defined following (5.5). This symmetry also holds for $\epsilon = 0$, along with the simpler symmetry $(b', v', v_0, S_s) \leftrightarrow (-b', -v', v_0, -S_s)$ discussed in § 4.

The generalization of the v' evaluation (4.6) is

$$v' = -\int_{-\infty}^{x} \left[\partial_z \left(\frac{b'}{N^2} \right) + \frac{S_s}{N^2} \partial_z v_0 + \epsilon S_s \frac{\partial_x b'}{N^2} \right] \mathrm{d}x'. \quad (5.3)$$

The parcel-displacement evaluations (4.1)–(4.2) are unchanged. Thus, the fields v', ζ', ξ' and χ' can be evaluated explicitly once the solution for b' is available.

Finite-ϵ wave-adjustment solutions are rather similar to the leading-order solutions in § 4. They are illustrated in figures 12 and 13 for a front and filament, respectively. There is remarkably little change in the peak amplitudes of b' and v', even for ϵ as large as 2, but their patterns are deformed by tilting leftward toward negative x while descending from the surface in comparison with the adjustment fields for $\epsilon = 0$ in figures 6–7. Similar behaviour is found for the finite-ϵ effect with constant N (not shown). Notice that finite ϵ breaks the simple x-symmetry of wave-adjusted fronts and filaments, quite substantially in these examples. Because $\epsilon(b', v')$ are large compared to (b_0, v_0), the wave-adjusted states look very different from the geostrophic–hydrostatic initial states.

We can explain the tilt by rewriting (5.2)–(5.3) as

$$\partial_x^2 b' + (\partial_z + \epsilon S_s \partial_x)^2 \left(\frac{b'}{N^2} \right) = S_s \partial_x^2 v_0 - (\partial_z + \epsilon S_s \partial_x) \left(\frac{S_s}{N^2} \partial_x b_0 \right) \quad (5.4)$$

$$v' = -\int_{-\infty}^{x} \left[(\partial_z + \epsilon S_s \partial_x) \left(\frac{b'}{N^2} \right) + \frac{S_s}{N^2} \partial_x b_0 \right] \mathrm{d}x'. \quad (5.5)$$

Notice that this system only has the derivatives ∂_x and $\partial_\gamma = \partial_z + \epsilon S_s(z) \partial_x$. In this regard (5.5) is isomorphic to the $\epsilon = 0$ system in § 4 except that the derivatives are transformed from the orthogonal (x, z) coordinates to the non-orthogonal (x, γ). The isomorphism is not complete, however, because the right-side field b_0 remains a function of (x, z), rather than (x, γ). Nevertheless, a line passing through the origin

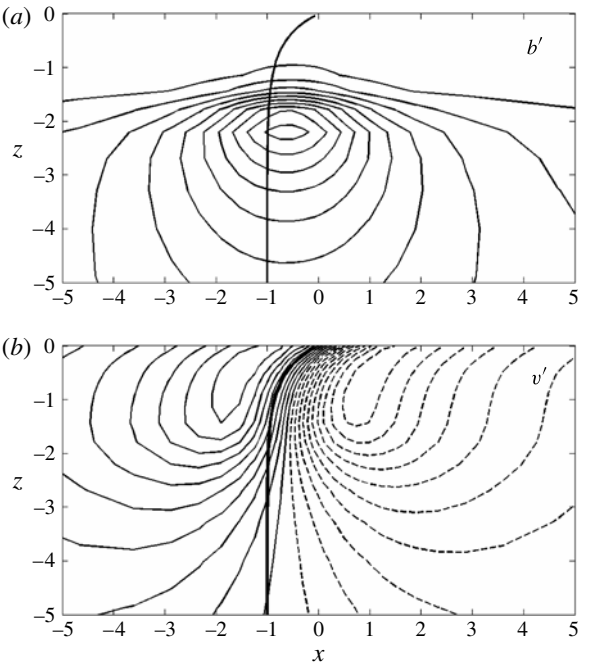

FIGURE 12. Wave-adjustment fields for the front (4.8) with the same parameters and stratification as in figure 6 except for $\epsilon = 2$. The fields are normalized by their extreme magnitudes (i.e. 8.8 and 6.8, respectively) and contoured as before. Stokes drift is directed toward positive y. The dark solid line is the γ coordinate axis passing through the origin; see (5.7).

in (x, z) and everywhere tangent to the unit vector

$$\hat{\boldsymbol{\gamma}} \equiv |\partial_\gamma \boldsymbol{x}|^{-1}(\partial_\gamma x\hat{\boldsymbol{x}} + \partial_\gamma z\hat{\boldsymbol{z}}) = J^{-1/2}(\epsilon S_s(z)\hat{\boldsymbol{x}} + \hat{\boldsymbol{z}}), \tag{5.6}$$

with $J = 1 + \epsilon^2 S_s^2$, *viz.*

$$x(z) = -\epsilon \int_z^0 S_s(z')\,\mathrm{d}z' = \frac{\epsilon}{\lambda}(\mathrm{e}^{\lambda z} - 1), \tag{5.7}$$

defines an approximate x symmetry line in (b', v') for finite ϵ (figures 12–13), replacing the exact $x = 0$ symmetry line for $\epsilon = 0$. However, this line is somewhat of an overestimate of the degree of leftward shift of the extrema in b' and v'. The line does show the same tilt as the isolines of v' through the mixed layer for both front and filament, whereas these isolines are nearly vertical with $\epsilon = 0$ (figures 6–7).

6. Summary and discussion

Surface fronts and filaments are inviscid steady states in geostrophic, hydrostatic balance in the absence of surface gravity waves. They can adjust conservatively to accommodate the Stokes drift vortex and Coriolis forces from gravity waves in a new steady balanced state. The wave-adjusted perturbation fields comprise two parts. One part is a horizontally uniform, anti-Stokes Eulerian flow that preserves the initial Lagrangian mean flow after adjustment. In the absence of a front, filament, or other flow structure to provide balancing forces for the Stokes–Coriolis effect, a

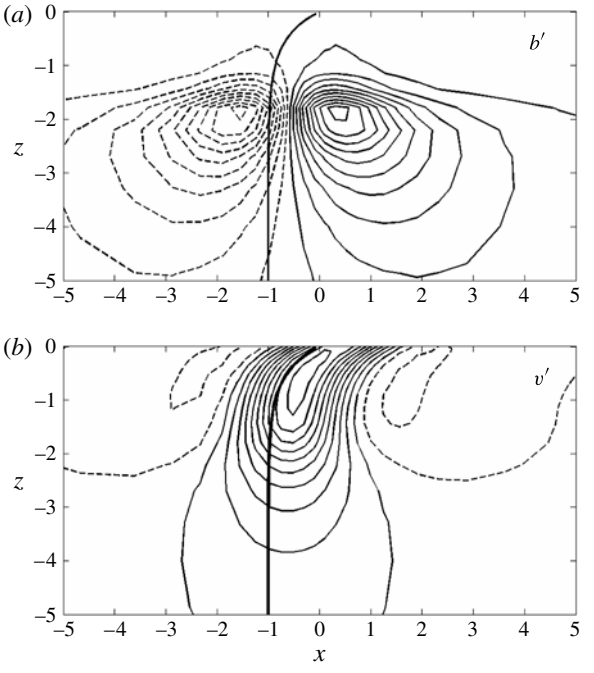

FIGURE 13. Wave-adjustment fields for the cold filament (4.11) with the same parameters and stratification as in figure 7 except for $\epsilon = 2$. The fields are normalized by their extreme magnitudes (i.e. 4.1 and 11.2, respectively) and contoured as before. Stokes drift is directed toward positive y. The dark solid line is the γ coordinate axis passing through the origin; see (5.7).

complete anti-Stokes flow would result. The other part is a localized adjustment in the neighbourhood of a front or filament that has the opposite horizontal symmetry from the initial fields (to leading order in ϵ) and thus induces a change of shape in the buoyancy and flow fields. The local wave-adjustment magnitude is relatively small for a uniformly stratified ocean, but it can be quite large for a mixed-layer stratification somewhat deeper than the vertical scale of the initial fields (i.e. the sweet-spot condition). For typical Stokes drift profiles that are stronger than the initial flow and have a shallower vertical scale, the parameter ϵ is not necessarily small, and fronts and filaments lose their horizontal symmetry during adjustment. The wave adjustment problem is posed for an arbitrary Rossby number $\mathscr{R}$, but solutions are obtained here only for $\mathscr{R} \ll 1$, i.e. more representative of the mesoscale and larger submesoscale than of the strongest submesoscale fronts and filaments.

In the ocean, fronts and filaments are more likely to be found in an already adjusted state than actively undergoing adjustment to suddenly arriving surface waves (which would be completed in a short interval of order $f^{-1} \approx$ h). This means that the before-and-after shape comparisons exploited here will usually not be available from measurements. Rather, an observational validation of wave-balanced adjustment is best done by diagnosing the force balances in the local buoyancy and flow fields: significant Stokes vortex and Coriolis forces within the thin Stokes layer and thermal wind balance below. Field detection is further complicated by the usual presence of active boundary layer turbulence (e.g. a wind-driven Ekman layer), so non-conservative

evolution will be occurring in addition to the conservative adjustment process analysed here. Furthermore, in the presence of waves, Langmuir turbulence in the boundary layer enhances the non-conservative effects in the wind-driven mean momentum balance (McWilliams *et al.* 1997; D'Asaro 2001). For this reason, the conservative wave-adjusted state may best be observed under solar restratification or swell without winds, so that the turbulent mixing plays a subdominant role. Furthermore, when the wave adjustment response is large because the mixed-layer stratification is weak, it may induce static instability and initiate further turbulence and non-conservative evolution. We commented above that sometimes the wave adjustment tends to oppose the effects of up-front and down-front winds. Clearly, observing general overturning and mixing is not sufficient to distinguish these competing processes. These complications go beyond the idealized problems solved here, and they are better explored in numerical large-eddy simulations with full wave-averaged dynamics (e.g. an initial frontal flow in the presence of a slowly growing wave field and boundary layer turbulence) that need not be restricted in the values of ϵ and $\mathscr{R}$ and that fully incorporate non-conservative boundary layer forcing and mixing processes.

It is still uncommon for surface gravity wave effects to be included in realistic oceanic circulation models, although prototypes exist (e.g. Uchiyama, McWilliams & Shchepetkin 2010) and there are cogent reasons for doing so (Cavaleri, Fox-Kemper & Hemer 2012) even beyond their classic roles in generating littoral currents through surf-zone breaking and Langmuir circulations in the Ekman layer through the vortex force. However, as modellers embark on this path, in particular by including the Stokes vortex and Coriolis forces featured here, several cautions about the requisite model spatial resolution and dynamics should be stated. Even at the larger scale of basin currents and mesoscale eddies, the anti-Stokes flow from the Stokes Coriolis force will be significant relative to other surface-layer currents. The effects of the Stokes vortex force are increasingly important on the smaller mesoscales and submesoscales, as ℓ decreases and ϵ and $\mathscr{R}$ increase, and where fronts and filaments arise in nature. As shown here, the dominant balances involve important ageostrophic and even non-hydrostatic dynamics. Most circulation models are hydrostatic, although it may often be sufficient to generalize them to a quasi-hydrostatic balance, i.e. one that includes the Stokes forces and even the non-traditional Coriolis force (the full three-dimensional $2\boldsymbol{\Omega} \times (\boldsymbol{u} + \boldsymbol{u}_s)$ of Earth's rotation vector) while still neglecting vertical acceleration. Such a procedure would allow for the equilibrated state studied here, but the internal waves generated in time-varying or initial-value problems may be more fundamentally non-hydrostatic. Clearly, direct simulation of the wave effects of Langmuir turbulence and wave breaking requires a non-hydrostatic model. Finally, fronts and filaments are often unstable to submesoscale fluctuations even while undergoing active sharpening through strain-induced frontogenesis (Fox-Kemper, Ferrari & Hallberg 2008; McWilliams, Molemaker & Olafsdottir 2009), and we remark that as yet no three-dimensional stability analysis has been made for a basic flow and stratification satisfying the wave-balanced constraints presented here, although a symmetric instability problem has recently been solved with wave effects (Li *et al.* 2012).

Because μ and $\epsilon/\mathscr{R}$ are usually not small in the ocean (figure 1), how much of our present dynamical understanding of geostrophic, hydrostatic flows needs to be reconsidered? Only near the surface are flows within the direct vertical domain of influence of the Stokes-drift forces, although the adjustment solutions here and Langmuir turbulence more generally (e.g. Polton & Belcher 2007) show that the domain extends deeper than the Stokes vertical scale h_s. For $\epsilon = \mathscr{R} = 0$, the flow

satisfies a 'Lagrangian thermal wind' balance wherein the same sea-level η and buoyancy distribution $b^{\dagger}$ are valid with or without waves for an Eulerian flow $\boldsymbol{u}$ that is altered only by the subtraction of an anti-Stokes flow, $\boldsymbol{u} \to \boldsymbol{u} - \boldsymbol{u}_s$; nevertheless, this Lagrangian remapping does not provide a dynamical isomorphism because the potential vorticity q and surface boundary conditions involve only the Eulerian velocity ($\boldsymbol{u}$), not the Lagrangian one ($\boldsymbol{u} + \boldsymbol{u}_s$). Most oceanic 'measurements' of larger-scale velocity – sea-level and hydrographic profile gradients, water mass tracer analysis, drifter trajectories, radar backscatter off surface waves – are more reflective of Lagrangian velocity than Eulerian. Therefore, although the magnitude of wave effects will not always be large, and their observational detection is often subtle, their influence may matter for a variety of upper-oceanic situations that should be reconsidered on a case-by-case basis.

Acknowledgements

We thank A. Tandon for early discussions about the possibility of wave-balanced flows. Discussions with R. Milliff, E. D'Asaro, G. Chini, W. Large and K. Julien helped to clarify the scope of the paper. This research is sponsored by ONR (N00014-11-1-0726) and NSF (DMS-0723757) for JCM and NSF (CMG-0934737) and NASA (NNX09AF38G) for BFK. The altimeter products were produced by Ssalto/Duacs and distributed by AVISO, with support from CNES (http://www.aviso.oceanobs.com/duacs/).

REFERENCES

BOYD, J. P. 2000 *Chebyshev and Fourier Spectral Methods*. Dover.

DE BOYER MONTÉGUT, C., FISCHER, G., LAZAR, A. S. & IUDICONE, D. 2004 Mixed layer depth over the global ocean: an examination of profile data and a profile-based climatology. *J. Geophys. Res.* **109**, C12003.

CAVALERI, L., FOX-KEMPER, B. & HEMER, M. 2012 Wind waves in the coupled climate system. *J. Geophys. Res. Bull. Am. Meteorol. Soc.* **93**, 1651–1661.

CRAIK, A. D. D. & LEIBOVICH, S. 1976 A rational model for Langmuir circulation. *J. Fluid Mech.* **73**, 401–426.

D'ASARO, E. A. 2001 Turbulent vertical kinetic energy in the ocean mixed layer. *J. Phys. Oceanogr.* **31**, 3530–3537.

FOX-KEMPER, B., FERRARI, R. & HALLBERG, R. W. 2008 Parameterization of mixed layer eddies. Part 1. Theory and diagnosis. *J. Phys. Oceanogr.* **38**, 1145–1165.

GENT, P. R. & MCWILLIAMS, J. C. 1983 Consistent balanced models in bounded and periodic domains. *Dyn. Atmos. Oceans* **7**, 67–93.

GJAJA, I. & HOLM, D. D. 1996 Self-consistent Hamiltonian dynamics of wave mean-flow interaction for a rotating stratified incompressible fluid. *Physica* D **98**, 343–378.

GUENTHER, R. & LEE, J. W. 1996 *Partial Differential Equations of Mathematical Physics and Integral Equations*. Dover.

HAMLINGTON, P. E., ROEKEL, L. P. VAN, FOX-KEMPER, B. & JULIEN, K. 2013 Langmuir–submesoscale interactions: descriptive analysis of multiscale simulations. *J. Phys. Oceanogr.* (submitted).

LEIBOVICH, S. 1983 The form and dynamics of Langmuir circulations. *Annu. Rev. Fluid Mech.* **15**, 391–427.

LI, K., ZHANG, Z., CHINI, G. & FLIERL, G. 2012 Langmuir circulation: an agent for vertical restratification? *J. Phys. Oceanogr.* **42**, 1945–1958.

LIN, S. J. & PIERREHUMBERT, R. T. 1988 Does Ekman friction suppress baroclinic instability? *J. Atmos. Sci.* **45**, 2920–2933.

McWILLIAMS, J. C. 2006 *Fundamentals of Geophysical Fluid Dynamics*. Cambridge University Press.

McWILLIAMS, J. C., MOLEMAKER, M. J. & OLAFSDOTTIR, E. I. 2009 Linear fluctuation growth during frontogenesis. *J. Phys. Oceanogr.* **39**, 3111–3129.

McWILLIAMS, J. C., RESTREPO, J. M. & LANE, E. M. 2004 An asymptotic theory for the interaction of waves and currents in coastal waters. *J. Fluid Mech.* **511**, 135–178.

McWILLIAMS, J. C., SULLIVAN, P. P. & MOENG, C. H. 1997 Langmuir turbulence in the ocean. *J. Fluid Mech.* **334**, 1–30.

POLTON, J. A. & BELCHER, S. E. 2007 Langmuir turbulence and deeply penetrating jets in an unstratified mixed layer. *J. Geophys. Res.* **112**, C09020.

THOMAS, L. N. 2005 Destruction of potential vorticity by winds. *J. Phys. Oceanogr.* **35**, 2457–2466.

UCHIYAMA, Y., McWILLIAMS, J. C. & SHCHEPETKIN, A. F. 2010 Wave–current interaction in an oceanic circulation model with a vortex-force formalism: application to the surf zone. *Ocean Model.* **34**, 16–35.

WEBB, A. & FOX-KEMPER, B. 2011 Wave spectral moments and Stokes drift estimation. *Ocean Model.* **40**, 273–288.